Subsurface hydrogen storage controlled by small-scale rock heterogeneities

Jangda, Zaid; Menke, Hannah; Busch, Andreas; Geiger, Sebastian; Bultreys, Tom; Singh, Kamaljit

DOI
10.1016/j.ijhydene.2024.02.233

Publication date
2024

Document Version
Final published version

Published in
International Journal of Hydrogen Energy

International Journal of Hydrogen Energy 60 (2024) 1192–1202

Contents lists available at ScienceDirect

International Journal of Hydrogen Energy

journal homepage: www.elsevier.com/locate/he

Subsurface hydrogen storage controlled by small-scale rock heterogeneities

Zaid Jangda [a,*], Hannah Menke [a], Andreas Busch [b], Sebastian Geiger [c], Tom Bultreys [d], Kamaljit Singh [a]

[a] Institute of GeoEnergy Engineering, Heriot-Watt University, EH14 4AS, Edinburgh, United Kingdom
[b] Lyell Centre, Heriot-Watt University, EH14 4AS, Edinburgh, United Kingdom
[c] Department of Geoscience and Engineering, Delft University of Technology, 2628, CN Delft, Netherlands
[d] UGCT/PProGRess, Department of Geology, Ghent University, 9000, Ghent, Belgium

ARTICLE INFO

Handling Editor: Dr Mehran Rezaei

Keywords:
Hydrogen storage
Porous media
Energy transition
Pore-scale 3D visualization

ABSTRACT

Subsurface porous rocks hold significant hydrogen (H_2) storage potential to support an H_2-based energy future. Understanding H_2 flow and trapping in subsurface rocks is crucial to reliably evaluate their storage efficiency. In this work, we perform cyclic H_2 flow visualization experiments on a layered rock sample with varying pore and throat sizes. During drainage, H_2 follows a path consisting of large pores and throats, through a low permeability rock layer, substantially reducing H_2 storage capacity. Moreover, due to the rock heterogeneity and depending on the experimental flow strategy, imbibition unexpectedly results in higher H_2 saturation compared to drainage. These results emphasize that small-scale rock heterogeneity, which is often unaccounted for in reservoir-scale models, plays a vital role in H_2 displacement and trapping in subsurface porous media, with implications for efficient storage strategies.

1. Introduction

With the increasing global demand for clean and sustainable energy sources, H_2 has emerged as a promising solution as a low-emission energy-carrier [1,2], particularly for hard to electrify decarbonizing sectors like heavy industry, long-haul transportation, and seasonal storage [3]. The surge in the worldwide interest in H_2 is evident from the announcement of more than 1000 large-scale H_2 production, supply, and infrastructure projects globally, with over 75% of them targeting full or partial commissioning by 2030 [4]. These projects represent a total of $320 billion in announced investments [4]. It is predicted that if clean H_2 is scaled up globally, the H_2 industry has the potential to generate $2.5 trillion in annual revenues and 30 million jobs, along with 20% global emissions reductions by 2050 [5]. Therefore, the demand for H_2 is expected to be substantial, with estimates reaching 2500 TWh for Europe by 2050 [6]. To accommodate such a demand, efficient H_2 storage solutions are essential, with projected storage requirements of 250–1000 TWh in Europe by 2050 [6] and potentially several gigatons globally [7]. Batteries and aboveground or sub-surface storage vessels can provide temporary H_2 storage solution, but their capacity is limited [8]. Subsurface storage of H_2 is therefore seen as a long-term storage solution as vast volumes of H_2 can be stored and produced when required.

Several types of underground hydrogen storage (UHS) systems are being considered both for short-term and long-term storage. The main options being salt caverns, depleted oil & gas reservoirs, and saline aquifers. Salt caverns have the highest deliverability and minimal risks of H_2 contamination [8], but the capacity is much lower compared to depleted gas reservoirs or saline aquifers [9,10]. Underground storage in depleted hydrocarbon reservoirs or aquifers emerges as a potential solution that provides the required storage capacity for these immense volumes of H_2 [2,9,11–13]. However, for the successful implementation of UHS in porous reservoirs, it is crucial to understand the displacement of H_2 during injection and withdrawal cycles [14–19]. To develop this understanding, it is important to analyze and quantify the interactions between H_2, the subsurface rocks and fluids and investigate the intricate pore-scale mechanisms that control H_2 displacement within these subsurface rocks [7,20–24].

Experimental studies conducted to understand these pore-scale phenomena have provided initial insights into the flow, transport, and trapping of H_2 in sandstone rocks. Wettability studies have generally concluded that water-wet conditions would prevail in an H_2-brine

* Corresponding author.
E-mail addresses: zaid.jangda@hw.ac.uk (Z. Jangda), h.menke@hw.ac.uk (H. Menke), a.busch@hw.ac.uk (A. Busch), s.geiger@tudelft.nl (S. Geiger), tom.bultreys@ugent.be (T. Bultreys), k.singh@hw.ac.uk (K. Singh).

https://doi.org/10.1016/j.ijhydene.2024.02.233
Received 11 December 2023; Received in revised form 17 January 2024; Accepted 17 February 2024
Available online 26 February 2024

system [21,22,25–30]. Recently, pore-scale fluid imaging experiments have been conducted to visualize and quantify the H_2 saturations and different pore-scale mechanisms occurring within rocks during and after H_2 injection and withdrawal. Results from these studies show that there will be a loss of H_2 in the subsurface due to capillary trapping [15,22,29,31], potential dissolution of H_2 in the imbibing brine [22], and that re-arrangement of H_2 could occur in the pore-space due to Ostwald ripening [7,32]. These studies offer valuable insights into the pore-scale phenomena that would arise during the implementation of large-scale UHS. However, it is important to note that almost all these investigations were conducted on homogeneous rocks and (except [22]) were not carried out under representative subsurface temperature and pressure conditions.

Most subsurface reservoirs are heterogeneous, meaning that pore and throat sizes, porosity, and permeability vary over a wide range of magnitudes and length scales [33–37]. In heterogeneous rocks, capillary pressure effects arise at boundaries between regions with distinctly different properties, i.e., with different permeability or porosity [35,38,39]. Heterogeneity in a geological formation can promote channeling of fluid flow along preferential flow paths that have high permeability, which leads to the bypassing of potentially large reservoir volumes and more complex displacement patterns [33,35,36,40–42]. Even small variations in permeability can alter fluid displacement patterns considerably [35,43]. Results from core-scale experiments showed that in a heterogeneous rock, the formation of high water saturation channels during imbibition could result in significant H_2 trapping during H_2 withdrawal, as a portion of the H_2 phase may be bypassed [41]. Results from a recent two-dimensional micromodel study [44] show that the change of flow direction from coarse to fine and fine to coarse sections of the micromodel significantly influenced the trend of the averaged capillary pressure curves and the remaining fluid saturation. Permeability heterogeneity is also expected to play a role in H_2 entrapment and recovery efficiency at the reservoir scale, with a recent simulation study showing 7% incremental H_2 recovery from a homogeneous reservoir compared to a heterogeneous reservoir [45]. Pore-scale heterogeneity is hence expected to play a critical role in both, the storage capacity of H_2 and the volume of H_2 that could be produced back from subsurface storage systems.

In this study, we address the challenge of understanding the effect of pore-scale heterogeneity on H_2 flow and trapping at subsurface temperature and pressure conditions. We performed H_2 flow experiments using a heterogeneous layered sandstone rock to investigate the impact of pore-scale heterogeneity on H_2 displacement and trapping. The experiments were carried out at temperature and pressure conditions of 50 °C and 10 MPa respectively, using a custom-designed flow apparatus, with the rock imaged *in situ* in an X-ray micro-computed tomography (μCT) scanner. We conducted two separate experiments to replicate two different scenarios that could arise during H_2 injection (a drainage process) and withdrawal (an imbibition process) from rock samples. Each experiment consisted of two cycles of drainage and imbibition. During drainage, H_2 was injected into the initially brine saturated rock sample from the top to simulate H_2 injection into a subsurface reservoir, while during imbibition, brine was injected from the bottom to simulate the displacement of stored H_2 during its withdrawal from a subsurface reservoir. After each fluid displacement step, we visualize and quantify the H_2 saturation in the rock and highlight the effect of pore-scale heterogeneity on fluid displacement.

The magnitude of the pore-scale heterogeneity present in the rock used for our experiments is generally not considered when developing reservoir-scale models [38], where permeability variations are usually incorporated when the difference is larger than an order of magnitude [37]. However, our findings emphasize that H_2 flow and trapping is highly influenced by subtle variations in the rock structure and properties, even for permeability contrasts lower than an order of magnitude. Furthermore, we emphasize variations in the fluid distributions based on the fluid injection strategy in each experiment performed in this work, further highlighting the impact of small-scale heterogeneity on H_2 flow and trapping behaviour.

2. Materials and methods

2.1. Materials and equipment

A cylindrical Clashach sandstone rock sample with a diameter of 6 mm and length of 12.4 mm was used as the porous medium for our experiments. Clashach is a quarried sandstone from Scotland, primarily consisting of approximately 90% quartz and 10% K-feldspar. Its permeability ranges from 2×10^{-13} to just over 1×10^{-12} m^2 and its porosity from 12 to 18% [46,47]. These values are similar to the properties of some reservoirs found in the North Sea [48–50]. Experimentally measured water permeability for the rock sample used for our experiments was found to be 1.1×10^{-12} m^2. Before starting the experiments, the rock sample was cleaned by immersing it in methanol under a fume hood for 20 h and then dried in a vacuum oven at 100 °C for 24 h. The rock sample was wrapped in Teflon tape and aluminum foil and placed inside a Viton sleeve. The Viton sleeve containing the rock sample was then wrapped with another layer of aluminum tape and an H_2 leak detection tape (Nitto) to identify any H_2 leakage around the rock sample during the experiments, before fitting inside a custom-designed rock core-holder (rs systems). The rock sample was not removed from the core-holder between the two set of experiments performed in this work. The core-holder was vertically fixed on a rotation stage inside an X-ray μCT scanner (EasyTom 150, RX Solutions) and connected to the flow system consisting of four syringe pumps (ISCO, three model 500D, and one model 100DX) and a Hastelloy reactor (Parr Instruments Company).

A brine solution (de-ionized water doped with 4 wt% potassium iodide to provide effective X-ray contrast) was used as the aqueous (wetting) phase and high purity (>99.99%) H_2 (supplied by BOC) was used as the gas (non-wetting) phase. The brine solution used for the saturation of the rock and imbibition was pre-equilibrated with H_2 at the experimental conditions in the Hastelloy reactor, to mitigate the loss of H_2 in the rock sample due to the potential dissolution of H_2 in the brine.

A differential pressure transducer (Keller, PD-33X) was added to the experimental setup to record the pressure difference between the top and bottom of the rock sample during all the fluid displacement steps. An additional flow line was also added to the bottom of the rock sample for the first of the two experiments. The schematic of the flow system is shown in Fig. 1.

2.2. Experimental procedure

The central vertical section of the rock sample was initially scanned using X-ray μCT before injecting any fluids. This dry scan served as a reference for the subsequent wet scans (containing H_2 and brine) taken after each fluid displacement step. The scanning parameters for all the scans are provided in Table S1 (Supplementary data).

For each of the two experiments performed in this work, CO_2 gas was first flushed through the rock sample at a pressure of 0.2 MPa to displace any air present in the rock sample. The CO_2 flush was followed by injection of 100 pore volumes (PV) of the non-equilibrated brine at a flow rate of 0.5 mL min^{-1} which was increased to 1 mL min^{-1}, to remove both the gaseous and dissolved CO_2 in brine, ensuring 100% brine saturation in the rock sample [51]. The pore pressure inside the rock sample and the confining pressure around the Viton sleeve were then gradually increased in steps of 0.2 MPa to the experimental pressure of 10 MPa and 12 MPa respectively. The rock sample was then heated to 50 °C and allowed to stabilize for 1 h. Next, the brine inside the rock sample was completely displaced with 70 PV of H_2-equilibrated brine from the reactor at a flow rate of 0.5 mL min^{-1} to achieve full saturation of the rock sample with H_2-equilibrated brine. To perform the fluid displacement steps (drainage and imbibition), low flow rates were used to ensure

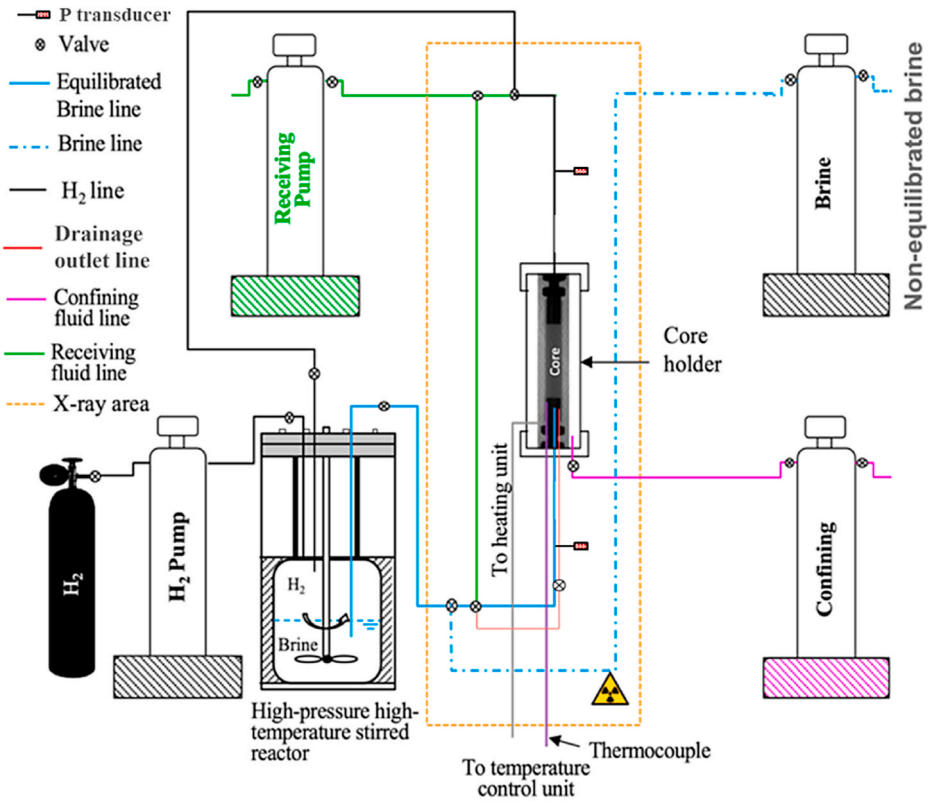

Fig. 1. Schematic of the flow system. An additional outlet line was added at the bottom of the rock sample for experiment 1, marked as the 'Drainage outlet line'.

that the displacements occur under capillary-dominated conditions, representative of field-scale flows [52]. H_2 was then injected (drainage) from the top of the rock sample at a flow rate of 0.05 mL min^{-1}, corresponding to a capillary number (Ca) of 4.2×10^{-9}. Here, $Ca = \mu v / \gamma$, where μ is the viscosity of H_2 (9.64×10^{-6} $Pa.s$) [53], v is the velocity of the injected H_2 (2.95×10^{-5} $m.s^{-1}$), and γ is the interfacial tension between H_2 and water (0.0683 $N.m^{-1}$) [54] at the experimental conditions of 50 °C and 10 MPa.

H_2 injection was stopped after 15 PV and the rock sample was scanned. Following this, 5 PV of brine was injected (imbibition) from the bottom of the rock sample to displace the H_2 at the same flow rate of 0.05 mL min^{-1}, corresponding to a Ca of 2.3×10^{-7}. Another scan was acquired after this displacement step. This drainage-scan-imbibition-scan cycle was then repeated. All the scans were conducted immediately after the completion of a fluid displacement step. Figs. 2 and 3 show the schematic of the experimental steps for each of the two experimental strategies used in this work which are explained in section 2.3.

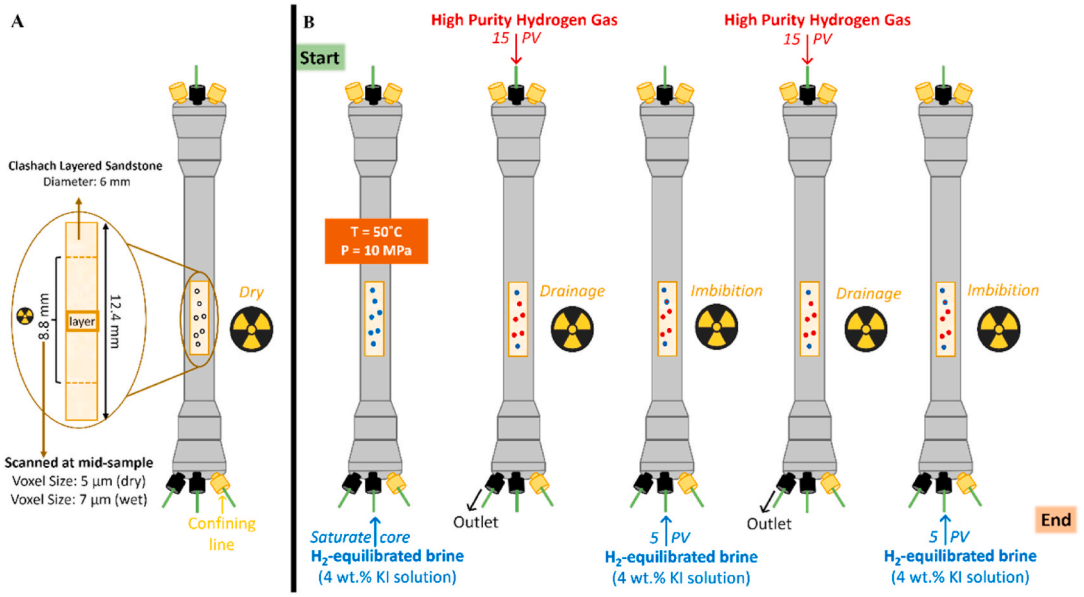

Fig. 2. Experimental steps (experiment 1). (A) the rock sample was initially scanned as dry and then (B) after each fluid displacement step.

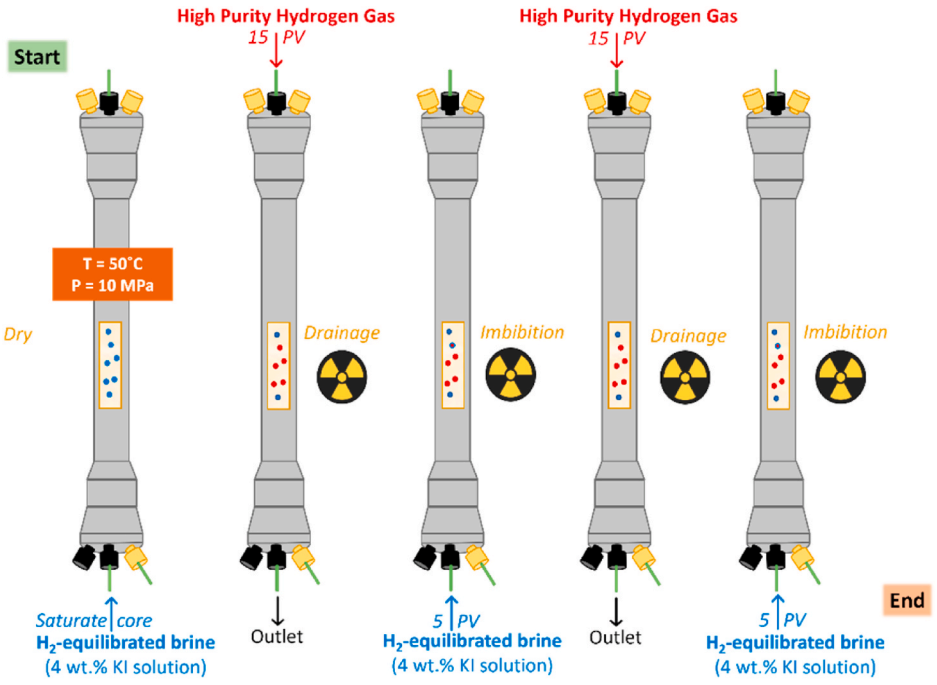

Fig. 3. Experimental steps (experiment 2). the rock sample scanned after each fluid displacement step.

2.3. Experimental strategies

Two separate experimental strategies were used. In the first strategy (in experiment 1), the rock was connected to two flowlines at the bottom of the rock sample (Fig. 4A and B).

When the rock sample was initially saturated with H_2-equilibrated brine, both flow lines were filled with this brine. During drainage, when H_2 was injected into the rock sample from the top, one flowline at the bottom allowed the flow of brine and H_2 to the receiving pump, while the second flowline remained filled with brine (Fig. 4A). This second flowline was then used to inject brine from the bottom during imbibition (Fig. 4B). This setup ensured that there was no dead volume of H_2 in the flow line which would get injected into the rock sample during imbibition.

In the second strategy (in experiment 2), only one flowline was connected to the bottom of the rock sample, serving as the outlet during drainage (Fig. 4C) and the inlet during imbibition (Fig. 4D). Consequently, the H_2 that accumulated in the bottom flowline during drainage was reintroduced into the rock sample at the commencement of brine injection. The slight variation in the experimental technique, which is generally used for experiments conducted on homogeneous rock samples [22], significantly influenced the fluid distributions, due to the inherent heterogeneity present in the rock sample, as discussed in the results and discussion section.

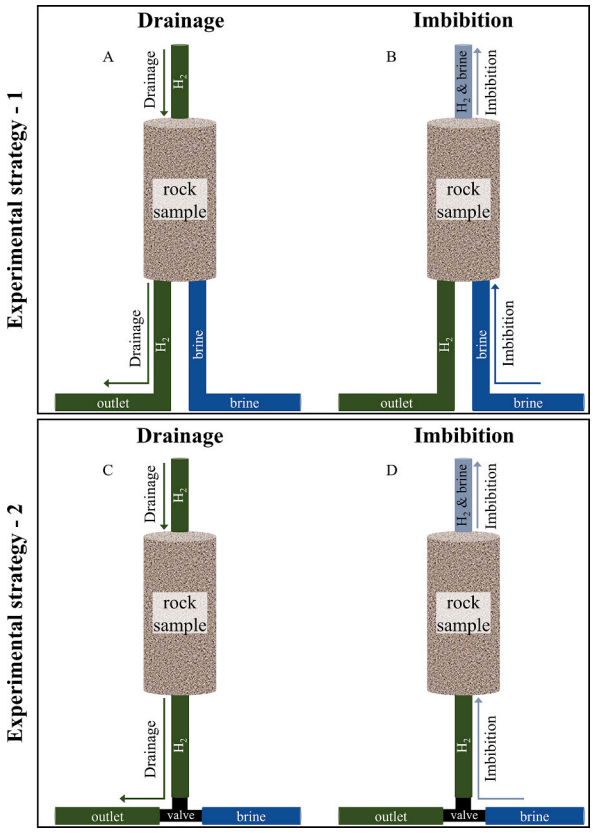

Fig. 4. A simplified visualization of the flow lines used for the two experiments. (A) & (B) show Experiment 1 in which two separate flowlines at the bottom of the rock sample were used, one for H_2 to flow out from the bottom of the rock sample during drainage (A) and another for brine injection into the rock sample during imbibition (B). (C) & (D) show Experiment 2 in which a single line was used for H_2 to flow out from the bottom of the rock sample during drainage (C) and for brine injection into the rock sample during imbibition (D).

2.4. Image processing and pore network extraction

The raw data from each scan was reconstructed using the EasyTom Xact software after which the images were processed using Avizo (ThermoFisher scientific) software. To visualize a longer length of the rock sample, the dry rock sample was scanned (at a voxel size of 5 μm) at two different heights. These two images were then stitched together resulting in the visualization of an 11.6 mm long central vertical section of the rock sample. From this stitched image, a sub-volume corresponding to a length of 8.8 mm was selected to be scanned (at a voxel size of 7 μm) for all the wet scans. The voxel size was increased for the wet scans to ensure that we could image the fluid displacement in layers of varying pore and throat sizes within the rock sample in a single scan,

while maintaining a good image resolution.

The image from the dry scan was resampled to match the length and voxel grid of the wet scans. Thereafter, all the images from the wet scans were registered to the image from the dry scan. A sub-volume corresponding to a length of 8.44 mm was selected for qualitative and quantitative analysis. All the images were then filtered using a non-local means filter [55] to remove noise. Image segmentation was then performed on all the images using a watershed algorithm [56] based on the grayscale intensity values. The image from the dry rock sample was segmented into rock grains and pores, while the H_2 phase was segmented from all wet scans. The segmented pores from the dry image served as a mask to obtain the brine phase for each of the H_2-segmented wet images. The image segmentation procedure is explained in detail in our previous work [22] and the threshold grayscale intensity values for each segmented image are provided in Table S2 (Supplementary data).

The segmented pore space from the dry scan was also used to extract a simplified pore network of the rock sample, consisting of spherical pores and throats. This pore network extraction was achieved through the application of the maximal ball algorithm [57–59], which allowed us to get the pore and throat size distributions and information about the pores and throats occupied by H_2 after each fluid displacement step (i.e., drainage and imbibition).

2.5. Layered analysis of the rock sample: bottom, middle, and top layers

In addition to analyzing the full sub-volume, we conducted a more detailed analysis of the rock sample by dividing it into three layers: bottom, middle, and top (Fig. 5A). This division was based on the average pore areas of the 2D vertical slices. To calculate these averages, we used the 2D area of each pore in every vertical slice. A central section, hereafter referred to as the middle layer, was selected by identifying consecutive slices with an average 2D pore area of less than 0.01 mm^2 (2D equivalent pore radius ~ 84 μm). This division allows for a comprehensive examination of the interplay of fluid flow and trapping behavior within each layer, owing to the variations in pore and throat sizes (and therefore porosity and permeability).

Table 1 shows the lengths, the average 3D pore and throat radii, and the permeabilities (obtained numerically from GeoChemFoam [60–62] using the Darcy-Brinkmann-Stokes (DBS) equation [63] solver) of each layer. The pore and throat size distributions are shown in Fig. S1 (Supplementary data).

Table 1
Lengths, pore, and throat radius (mean ± standard deviation) and permeability of the different layers of the core sample. Permeability values were obtained using the simpleFoam solver in GeoChemFoam 5.0

	Full sample	Bottom layer	Middle layer	Top layer
	0–8.44 mm	0–3.67 mm	3.67–5.11 mm	5.11–8.44 mm
	1207 slices	524 slices	206 slices	477 slices
Avg. pore radius (μm)	31 ± 12	35 ± 14	28 ± 10	30 ± 11
Avg. throat radius (μm)	15 ± 7	17 ± 8	14 ± 6	15 ± 7
Permeability (m^2)	1.0×10^{-12}	3.4×10^{-12}	5.1×10^{-13}	1.0×10^{-12}

These layers in the rock sample exhibit minor differences (<10 μm) in pore and throat radii. Even though the differences in the average pore and throat radii between the three layers are relatively small, they do exhibit permeability variations. Specifically, the bottom layer has a significantly higher permeability ($3.4 \times 10^{-12}\ m^2$) compared to the middle ($5.1 \times 10^{-13}\ m^2$) and top ($1.0 \times 10^{-12}\ m^2$) layers. Permeability variations of this magnitude and length-scales are challenging to upscale into large-scale reservoir models, and rocks containing small-scale heterogeneity are often grouped as a single hydraulic unit [37]. However, we observe that these small-scale heterogeneities contribute significantly to the H_2 movement and trapping in the rock sample.

Analysis of the 2D average pore area (represented by 2D equivalent pore radius in Fig. 5B) for each slice shows the presence of a layer in the middle of the rock sample characterized by smaller pores (Fig. 5B). When considering the 3D positions of all the pores and throats, we observe that the bottom layer consists of a significantly larger number of larger pores and throats (Fig. S2 in Supplementary data). While the middle layer consists mostly of relatively smaller pores and throats compared to the bottom and top layers, there are a few large pores and throats present in the middle layer. These large pores and throats in the middle layer are likely to provide an interconnected pathway, facilitating the initial flow of H_2 between the top and bottom layers as discussed in Section 3.

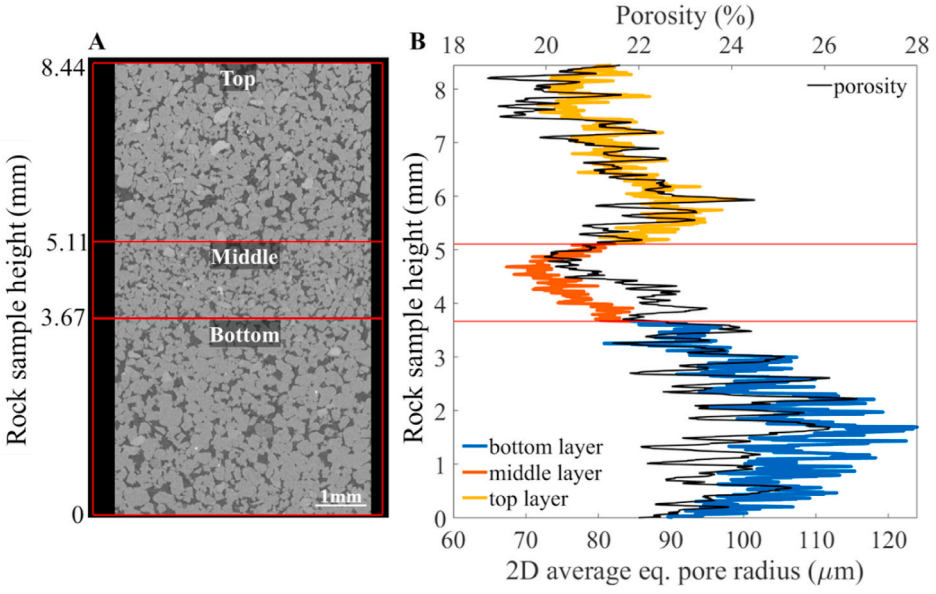

Fig. 5. Pore and throat size analysis. (A) 2D cross-section showing the rock sample divided into three layers with a visual difference in pore sizes, and (B) average equivalent (eq.) pore radius obtained from 2D average pore area for each 2D vertical slice plotted against the rock sample height. The variation of porosity along the sample is also shown.

3. Results and discussion

3.1. Experiment 1 – Dual flowlines at the bottom of the rock sample

In this experiment, the bottom of the rock sample was connected to two flowlines, one serving as the outlet during drainage and the other as the inlet during imbibition (Fig. 4A&B). Two cycles of drainage and imbibition were performed. During the first drainage step (in Cycle 1), the injected H_2 enters the top layer from above, invading the large throats, and stays as a connected phase (Fig. 6A).

When H_2 reaches the middle layer, the decrease in the number of connected flow paths through larger pores could cause a restriction to flow due to capillary forces [41], as a higher capillary pressure is needed to invade the middle layer consisting of smaller pores and throats. This flow restriction could result in the accumulation of H_2 just above the middle layer, increasing the H_2 saturation and the capillary pressure. The H_2 saturation after drainage in the full rock sample is 38% compared to a H_2 saturation of 60% in the top layer and 28% in the bottom layer. The 3D visualization of H_2 after drainage shows that H_2 is connected between the top and the bottom layer via a single channel (Fig. 6A). This connection indicates that H_2 flows through the path which requires the lowest capillary entry pressure within the middle layer. This path consists of throats larger than the average throat size in the middle layer (Fig. 7).

The flow of H_2 through the channel in the middle layer results in the H_2 bypassing most of the middle layer and an increase in H_2 saturation just below the middle layer. This observation aligns with findings in a 2D study [43] for an oil-water system, where channeling of the non-wetting phase was reported in a micromodel consisting of layers of varying throat sizes.

Brine is then injected from the bottom of the rock sample to displace the H_2. Since there are separate flow lines at the bottom for the H_2 outlet during drainage and brine inlet during imbibition, the brine directly enters the rock sample during imbibition and starts displacing H_2. The overall residual H_2 saturation after imbibition is 13%, showing a recovery factor of 66%. Even though the residual H_2 saturation in the top layer is higher compared to the full rock sample (Fig. 6J), the recovery trend is comparable. H_2 remains as small, disconnected ganglia throughout the rock sample (Fig. 6B and G) as an increase in the brine phase saturation leads to snap-off and trapping of H_2 in the larger pores. H_2 phase connectivity between the top and the bottom layer is also broken off with most of the H_2 ganglia trapped above and below the middle layer.

H_2 is then re-injected into the rock sample from the top (Cycle 2). The connectivity of H_2 occurs through the same channel as in the first drainage, bypassing most of the middle layer (Fig. 6C and 6H). The overall H_2 saturation of 38% after the second drainage is the same as the first drainage, however, further analysis shows that there is a difference in H_2 saturations in the top and bottom layers (Fig. 6J). H_2 saturation in the bottom layer after the second drainage is higher compared to the first drainage, likely due to the presence of residual H_2 clusters after the first imbibition.

Brine re-injection from the bottom for the second imbibition follows the second drainage step. Results show that the overall recovery factor of 47% for this cycle is lower compared to the recovery factor for the first cycle (66%). In the top layer, the H_2 saturation profiles are similar for both the imbibition steps, with a residual H_2 saturation of 23% and 26% after the first imbibition and the second imbibition respectively. However, in the bottom layer, the residual H_2 saturation of 21% is considerably higher after the second imbibition compared to 7% after the first imbibition. The higher saturation of H_2 in the bottom layer after the second drainage contributes to higher residual trapping of H_2 after the second imbibition. 3D visualization of H_2 (Fig. 6D) shows that the higher residual saturation in the bottom layer is due to the presence of a single large ganglion that contributes to over 70% of the residual H_2 saturation in the bottom layer (Figure S3 – Supplementary data). The trapping of a

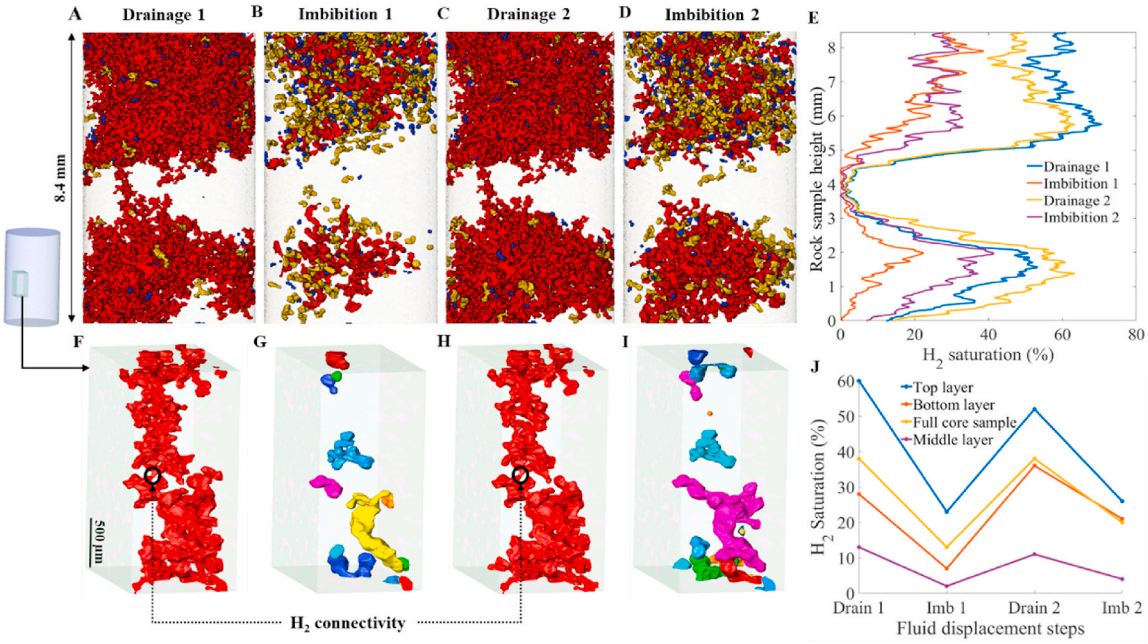

Fig. 6. H_2 saturation analysis (experiment 1). H_2 phase visualization inside the full rock sample after each fluid displacement step, (A) after first drainage, (B) after first imbibition, (C) after second drainage, and (D) after second imbibition. In (A)–(D), red colour represents connected H_2 phase occupying pore space larger than 100 times the average pore size, yellow colour represents connected H_2 phase occupying pore space between 10 and 100 times the average pore size and blue colour represents connected H_2 phase occupying pore space up to 10 times the average pore size, (E) H_2 saturation after each fluid displacement step plotted against the rock sample height. H_2 phase visualized in a subsection of the rock sample after each fluid displacement step, (F) and (H) after the first and second drainage respectively with the smallest throat providing the H_2 connection encircled, (G) and (I) after the first and second imbibition respectively showing trapped, disconnected H_2 ganglia after imbibition. (J) H_2 saturation values in the different layers of the rock sample after each fluid displacement step. (For interpretation of the references to colour in this figure legend, the reader is referred to the Web version of this article.)

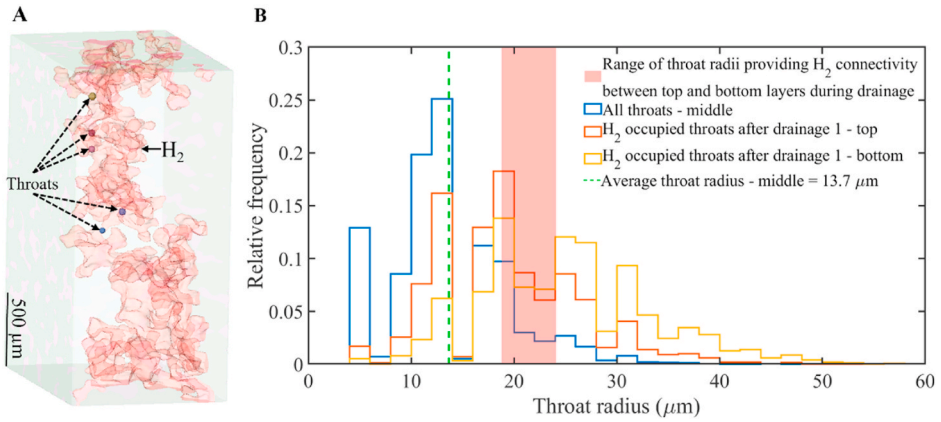

Fig. 7. Throat size analysis (experiment 1 – drainage). (A) a subsection of the rock sample with throats shown as spheres that allow for connectivity of H_2 phase (semi-transparent red) between the top and bottom layers during drainage, (B) throat size distributions of all throats in the middle layer and H_2 occupied throats in the top and bottom layers during the first drainage. The average throat radius of all the throats in the middle layer is marked as a dashed-green line and the throats present in the pathway providing the H_2 connectivity between the top and bottom layers during drainage are highlighted by the red-shaded region. (For interpretation of the references to colour in this figure legend, the reader is referred to the Web version of this article.)

large non-wetting phase ganglion during imbibition, resulting from throat size variation, has also been observed in 2D micromodel experiments for oil-water systems [43].

Pore and throat occupancy analysis for H_2 reveals a preferential filling of larger pores and throats (Fig. 8). However, due to the presence of larger pores and throats in the bottom layer (cf. Table 1), the average pore and throat radii of the H_2-filled pores in this layer were larger compared to the other layers. The difference in the sizes of the H_2 occupied pores and throats in the top layer and the average of the overall pores and throats of the top layer is smaller compared to the bottom layer. This relatively small difference between the average radii of all the pores and throats in the top layer and the H_2 occupied pores and throats in the top layer indicates that H_2 starts filling relatively smaller pores and throats within the top layer during drainage, which is caused by restriction to H_2 flow through the middle layer, until a connection through the middle layer is established for H_2 to flow into the bottom layer.

The average radii of the H_2 occupied pores and throats increase after imbibition (Fig. 8), indicating that brine occupies most of the smaller pores with H_2 left in the larger pores. Due to the higher H_2 residual saturation in the bottom layer after the second imbibition compared to the first imbibition, H_2 enters more of the smaller pores and throats in the bottom layer. As seen in Fig. 8B, the increase in the average throat radius of H_2 occupied throats for the second imbibition (from 27 to 29 μm) is significantly smaller compared to the first imbibition step (from 25 to 31 μm). Additionally, a much higher number of pores and throats are occupied by H_2 after the second imbibition compared to the first imbibition in the bottom layer. The number of pores and throats occupied by H_2 after each fluid displacement step in the different layers of the rock sample and the corresponding values of the average pore and throat radii are provided in Table S3 and Table S4 (Supplementary data).

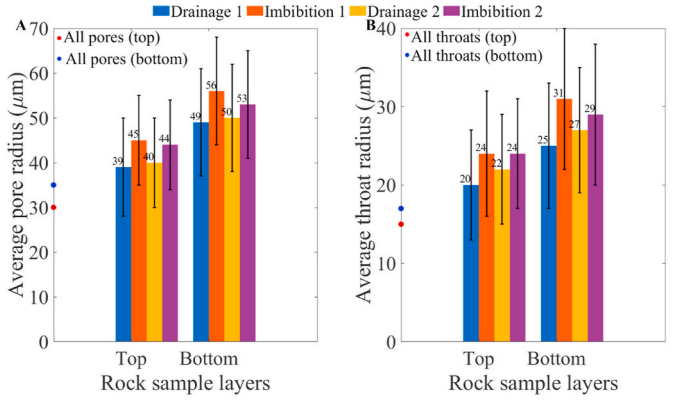

Fig. 8. (A) Average pore radius of H_2 occupied pores and (B) average throat radius of H_2 occupied throats after each fluid displacement step in the top and bottom layers of the rock sample. The red and blue filled symbols represent the average pore radius of all the pores in the top and bottom layers in (A) respectively and the average throat radius of all the throats in the top and bottom layers in (B) respectively. (For interpretation of the references to colour in this figure legend, the reader is referred to the Web version of this article.)

Overall, this cyclic H_2 injection and withdrawal experiment shows that the small-scale heterogeneities in the rock have a significant influence on the pore-scale fluid displacement and trapping during drainage and imbibition.

3.2. *Experiment 2 – single flowline at the bottom of the rock sample*

Using the same rock sample, we performed another experiment with a slight modification in the experimental apparatus. In this experiment, a single flowline was connected to the bottom of the rock sample (Fig. 4C&D). This flowline served as the outlet from the rock sample during drainage and the inlet to the rock sample during imbibition. This type of flowline configuration is mostly used in experiments conducted on homogeneous rock samples in which we observe uniform fluid distribution of the H_2 after drainage [22]. When the flow is reversed during imbibition, we do not expect the H_2 present in the flowline to enter additional pores that have remained filled with brine after drainage. However, for our experiment, due to the variation in the pore and throat sizes in different layers, the fluid configurations vary significantly with the change in injection strategy, and we observe H_2 occupying additional pores during imbibition (Fig. 9).

During the first drainage, H_2 fills the top layer of the rock sample (Fig. 9A) and bypasses the middle layer after breakthrough. After this drainage, the H_2 saturation is 53% in the top layer, while in the bottom layer, the H_2 saturation is 17% and confined to one side. The full rock sample has a H_2 saturation of 30%, which is lower than that in experiment 1, due to the low saturation in the bottom layer (see Fig. 9J). As described for experiment 1 in the previous section, the higher H_2 saturation in the top layer is possibly due to the higher local capillary pressure reached during drainage in the section upstream from the middle layer than in the section downstream of the middle layer because the middle layer has a higher capillary invasion pressure.

Subsequently, brine is injected from the bottom of the rock sample

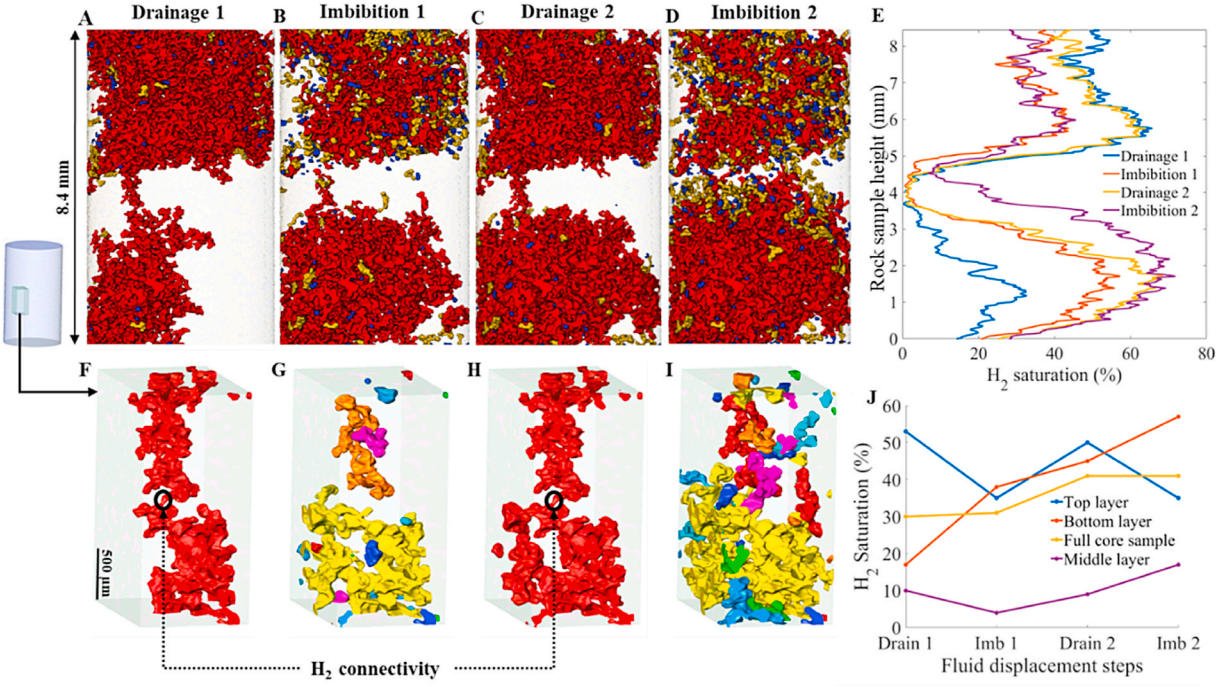

Fig. 9. H_2 saturation analysis (experiment 2). H_2 phase visualization inside the full rock sample after each fluid displacement step, (A) after first drainage, (B) after first imbibition, (C) after second drainage, and (D) after second imbibition. In (A)–(D), red colour represents connected H_2 phase occupying pore space larger than 100 times the average pore size, yellow colour represents connected H_2 phase occupying pore space between 10 and 100 times the average pore size and blue colour represents connected H_2 phase occupying pore space up to 10 times the average pore size, (E) H_2 saturation after each fluid displacement step plotted against the rock sample height. H_2 phase visualized in a subsection of the rock sample after each fluid displacement step, (F) and (H) after imbibition. (J) H_2 saturation values in the different layers of the rock sample after each fluid displacement step. (For interpretation of the references to colour in this figure legend, the reader is referred to the Web version of this article.)

during the first imbibition cycle. Following this fluid displacement step, we observe a notable increase in the H_2 saturation in the bottom layer of the rock sample, as it rises from 17% (after drainage) to 38% (after imbibition). This increase may be attributed to the presence of H_2 within the flowline, introducing an additional volume of H_2 into the rock sample from the bottom prior to imbibition. This additional volume of H_2 invades more pore space and increases the H_2 saturation in the bottom layer as this layer is now upstream to the middle layer, allowing the local capillary pressure in the bottom layer to increase. For a homogeneous sample, this change in the direction of H_2 injection would not increase the H_2 saturation, as the H_2 would flow through the already invaded pore space as there is no mechanism to increase the local capillary pressure.

During imbibition, it is likely that snap-off of the H_2 phase occurs in the middle layer (Fig. 9G) as it has smaller pores and throats, which are the first places to be invaded by brine. This snap-off results in the disconnection of the H_2 phase and forces the H_2 to accumulate below the middle layer, creating a drainage-like condition. We observe a slight increase in the overall H_2 saturation after the first imbibition which is 31% as compared to the first drainage (30%). The saturation profiles are opposite for the different layers of the rock sample, with H_2 saturation reducing from 53% to 35% in the top layer while increasing from 17% to 38% in the bottom layer (see Fig. 9E and J). As there is no restriction to flow in the top layer, only trapped H_2 ganglia are left after imbibition. All the additional H_2 accumulates in the bottom layer (Fig. 9B), emphasizing the role of the small changes in the pore and throat sizes on the fluid distributions and trapping.

The double displacement, i.e., reverse drainage process during imbibition, observed in the layered sample would not have occurred in a homogeneous rock sample and a similar recovery factor (in a completely homogeneous rock sample) would have been expected as in the top layer. The recovery factor of 34% for the top layer matches closely with the results from our previous experiment conducted on a homogeneous rock sample at the same conditions, using the same experimental strategy [22].

The second flow cycle is then initiated, and H_2 is re-injected from the top. In this drainage step, we observe a similar saturation profile in the top layer as in the first drainage step (Fig. 9E). The connecting path between the top and bottom layers remains the same for both drainage cycles (Fig. 9F and H) with most of the middle layer bypassed by H_2. H_2 saturation (after the second drainage) in the bottom layer is 45%, which is higher compared to the first drainage due to the high H_2 saturation obtained after the first imbibition.

Brine is then re-injected from the bottom for the second imbibition step. We observe that the H_2 saturation in the bottom layer further increases after the second imbibition, as additional H_2 in the flow line enters the rock sample from the bottom. Similar to that in the first cycle, it is likely that snap-off occurred in the middle layer during imbibition, breaking the H_2 connectivity between the top and bottom layers (Fig. 9I). The saturation profile in the top layer follows a similar trend to that of the first imbibition (Fig. 9E), with only trapped H_2 ganglia left in the pore space. For the second imbibition, we observe that H_2 invades relatively smaller pores and throats of the bottom layer and even part of the middle layer. The overall H_2 saturation is 41% which is the same as the overall saturation after the second drainage. The H_2 saturation reduces from 50% to 35% in the top layer and increases from 45% to 57% in the bottom layer after the second imbibition (see Fig. 9J). The top layer has the same residual H_2 saturation after the second imbibition as after the first imbibition and displays a saturation profile and recovery factor comparable to a homogeneous rock sample [22].

Overall, it is evident that the pore-scale heterogeneity in our rock sample strongly influences the H_2 saturation if the injection strategy is changed. For our rock sample, the top layer could present the closest representation of a homogenous rock, and if analyzed separately, shows

that the residual H_2 saturation does not increase after multiple cycles as reported in a recent study [15]. However, subsurface reservoirs generally exhibit structural heterogeneity and as observed in this study, even small-scale heterogeneities in the pore space of a layered rock sample have a substantial influence on the residual saturation of H_2.

The analysis of the H_2 pore occupancy is consistent with the saturation trend in the different layers of the rock sample as shown in Fig. 10. In the bottom layer, where H_2 saturation consistently increases throughout the fluid displacement steps, there is a corresponding increase in the number of H_2 occupied pores and throats from the first drainage up to the second imbibition (Fig. 10A). Additionally, as H_2 saturation increases with each fluid displacement step in the bottom layer, with H_2 invading more smaller pores and throats, we observe a decreasing trend in the average pore and throat radii of H_2 occupied pores and throats after each fluid displacement step (Fig. 10C and D). The number of pores and throats occupied by H_2 after each fluid displacement step in the different layers of the rock sample and the corresponding values of the average pore and throat radii are provided in Table S5 and Table S6 (Supplementary data).

Conversely, in the top layer, we observe that the number of H_2 occupied pores and throats is less after each imbibition step compared to the previous drainage step, and the average pore and throat radii of H_2-occupied pores and throats is higher after each imbibition step compared to the previous drainage step (Fig. 10B,C and D), which is similar to that observed in a homogeneous sample [22].

Pressure drop data measured across the rock sample shows spikes during drainage (Figure S4A – Supplementary data) which could be due to the flow restrictions in the middle layer of the rock sample. However, due to the small pore volume of the rock sample, the exact time when H_2 reached the middle layer is difficult to ascertain. A higher pressure drop observed during the second imbibition (Figure S4B – Supplementary data) is indicative of H_2 filling the middle layer, as we observe a higher saturation of H_2 in the middle layer after the second imbibition (Fig. 9D&E, and Fig. 9J).

4. Conclusions

Through this study, we offer valuable insights into the impact of pore-scale heterogeneity on H_2 displacement and trapping during UHS in subsurface reservoirs. We show that for low flowrate (capillary dominated) displacement experiments, capillary pressure effects complicate the fluid displacements, particularly near heterogeneous boundaries, and significantly influence the initial H_2 saturation and the subsequent trapping of H_2. We found that H_2 flows along a preferential pathway through a low permeability layer, bypassing a section of the rock sample, and thereby reducing the initial storage capacity. Our results also show that during H_2 withdrawal from a heterogeneous rock, a larger volume of H_2 could get trapped below low permeability layers due to snap-off events occurring in the smaller throats of the low permeability layer.

These findings show that heterogenous rocks behave differently from homogenous rocks. The small heterogeneities in pore and throat sizes, and permeabilities analyzed in this study show a surprising effect on flow, saturation, and trapping of H_2 in reservoir rocks. The impact of small-scale heterogeneities on UHS should be studied further through experiments using different capillary numbers and permeability contrasts. Furthermore, we emphasize the importance of the direction of fluid injection on H_2 distribution and trapping in a heterogeneous rock, whereby if any volume of H_2 enters the rock sample before the imbibing brine, the residual H_2 saturation could increase after imbibition compared to the initial H_2 saturation after drainage.

Performing time-resolved 3D visualization experiments could allow real-time visualization of H_2 snap-off events occurring within the heterogeneous layers of the rock sample, providing further insights into H_2 trapping, accumulation and displacement mechanisms. Understanding such pore-scale phenomena is crucial for informing and validating pore-scale models. While this work focuses on the pore-scale, it highlights the importance of considering small-scale heterogeneity, which is often overlooked in large-scale reservoir models, when designing and implementing UHS systems.

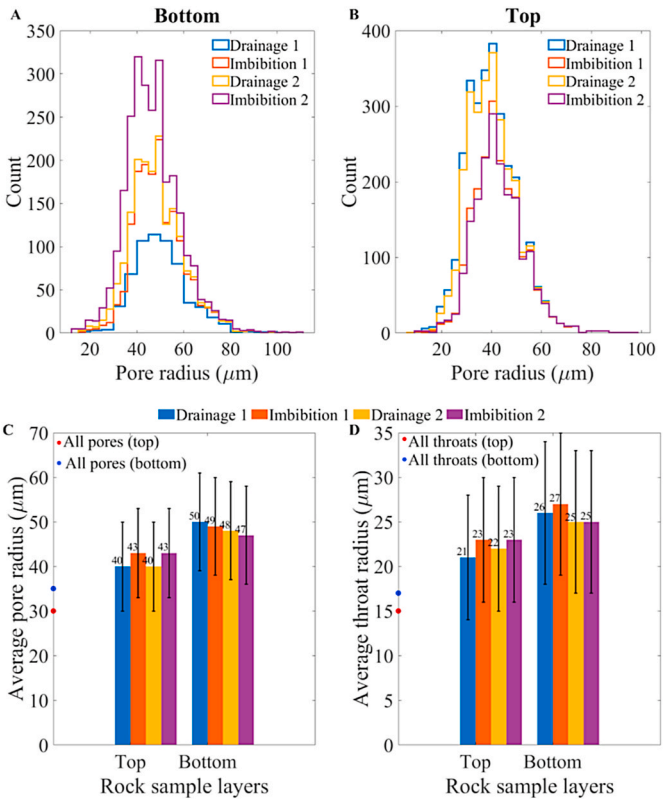

Fig. 10. Comparison of H_2 pore occupancy: (A) bottom layer after each displacement step shows that the number of pores occupied by H_2 increases in each subsequent fluid displacement step with the peak shifting towards the left, (B) top layer after each fluid displacement step shows that the number of H_2 occupied pores is higher after each drainage compared to each imbibition and the average pore radius of H_2 occupied pores is larger for imbibition steps compared to drainage steps. Additionally in the top layer, the plots for both the drainage steps match each other as do the plots for both the imbibition steps, (C) average pore radius of H_2 occupied pores and (D) average throat radius of H_2 occupied throats after each fluid displacement step in the top and bottom layers of the core sample. The red and blue filled symbols represent the average pore radius of all the pores in the top and bottom layers in (C) respectively and the average throat radius of all the throats in the top and bottom layers in (D) respectively. (For interpretation of the references to colour in this figure legend, the reader is referred to the Web version of this article.)

Data availability statement

The raw, filtered, and segmented tomographic datasets and the extracted pore and throat image files have been uploaded to a public repository (zenodo), the details of which are provided at https://doi.org/10.5281/zenodo.8375682.

Declaration of competing interest

The authors declare that they have no known competing financial interests or personal relationships that could have appeared to influence the work reported in this paper.

Acknowledgement

We thank Helen Lewis for providing access to the X-ray tomography

facility at the Institute of GeoEnergy Engineering at Heriot-Watt University and Mehran Sohrabi for providing the rock for these experiments. We gratefully acknowledge Jim Buckman, Clayton Magill, Paul Miller, Robert Louden, and Jim Allison for their support in the preparation of the equipment and materials used for our experiment. We are also thankful to Energi Simulation for providing partial funding for this research. Tom Bultreys acknowledges funding from the Research Foundation-Flanders (FWO) under grant numbers G004820N and 12X0922N.

Appendix A. Supplementary data

Supplementary data to this article can be found online at https://doi.org/10.1016/j.ijhydene.2024.02.233.

References

[1] Miocic J, Heinemann N, Edlmann K, Scafidi J, Molaei F, Alcalde J. Underground hydrogen storage: a review. Geol Soc, London, Special Publ Jul. 2023;528(1). https://doi.org/10.1144/sp528-2022-88.
[2] Heinemann N, et al. Enabling large-scale hydrogen storage in porous media-the scientific challenges. Energy Environ Sci Feb. 01, 2021;14(2):853–64. https://doi.org/10.1039/d0ee03536j.
[3] International Energy Agency. Global hydrogen review 2023 [Online]. Available: www.iea.org; 2023.
[4] Hydrogen Insights 2023 an update on the state of the global hydrogen economy, with a deep dive into North America. 2023 [Online]. Available: www.hydrogencouncil.com.
[5] U.S. National clean hydrogen strategy and roadmap. 2023. https://www.hydrogen.energy.gov/docs/hydrogenprogramlibraries/pdfs/us-national-clean-hydrogen-strategy-roadmap.pdf.
[6] Cavanagh A, Yousefi H, Wilkinson M, Groenenberg R. HyUSPRe Hydrogen Underground Storage in Porous Reservoirs - hydrogen storage potential of existing European gas storage sites in depleted gas fields and aquifers. The HyUSPRe consortium [Online]. Available: www.hyuspre.eu; 2024.
[7] Zhang Y, Bijeljic B, Gao Y, Goodarzi S, Foroughi S, Blunt MJ. Pore-scale observations of hydrogen trapping and migration in porous rock: demonstrating the effect of Ostwald ripening. Geophys Res Lett Apr. 2023;50(7). https://doi.org/10.1029/2022GL102383.
[8] Andersson J, Grönkvist S. Large-scale storage of hydrogen. Int J Hydrogen Energy May 2019;44(23):11901–19. https://doi.org/10.1016/J.IJHYDENE.2019.03.063.
[9] Zivar D, Kumar S, Foroozesh J. Underground hydrogen storage: a comprehensive review. Int J Hydrogen Energy Jul. 2021;46(45):23436–62. https://doi.org/10.1016/j.ijhydene.2020.08.138.
[10] Muhammed NS, Haq B, Al Shehri D, Al-Ahmed A, Rahman MM, Zaman E. A review on underground hydrogen storage: insight into geological sites, influencing factors and future outlook. Energy Rep Nov. 01, 2022;8:461–99. https://doi.org/10.1016/j.egyr.2021.12.002.
[11] Aftab A, Hassanpouryouzband A, Xie Q, Machuca LL, Sarmadivaleh M. Toward a fundamental understanding of geological hydrogen storage. Ind Eng Chem Res Mar. 09, 2022;61(9):3233–53. https://doi.org/10.1021/acs.iecr.1c04380.
[12] Jafari Raad SM, Leonenko Y, Hassanzadeh H. Hydrogen storage in saline aquifers: opportunities and challenges. Renew Sustain Energy Rev Oct. 2022;168:112846. https://doi.org/10.1016/J.RSER.2022.112846.
[13] Haddad PG, et al. Geological storage of hydrogen in deep aquifers - an experimental multidisciplinary study. Energy Environ Sci Jul. 2022;15(8):3400–15. https://doi.org/10.1039/d2ee00765g.
[14] Liu N, Kovscek AR, Fernø MA, Dopffel N. Pore-scale study of microbial hydrogen consumption and wettability alteration during underground hydrogen storage. Front Energy Res Feb. 2023;11. https://doi.org/10.3389/fenrg.2023.1124621.
[15] Thaysen EM, et al. Pore-scale imaging of hydrogen displacement and trapping in porous media. Int J Hydrogen Energy Jan. 2023;48(8):3091–106. https://doi.org/10.1016/j.ijhydene.2022.10.153.
[16] Esfandyari H, Sarmadivaleh M, Esmaeilzadeh F, Ali M, Iglauer S, Keshavarz A. Experimental evaluation of rock mineralogy on hydrogen-wettability: implications for hydrogen geo-storage. J Energy Storage 2022;52:104866. https://doi.org/10.1016/j.est.2022.104866.
[17] Hassanpouryouzband A, et al. Geological hydrogen storage: geochemical reactivity of hydrogen with sandstone reservoirs. ACS Energy Lett Jun. 2022:2203–10. https://doi.org/10.1021/acsenergylett.2c01024.
[18] Al-Yaseri A, Esteban L, Yekeen N, Giwelli A, Sarout J, Sarmadivaleh M. The effect of clay on initial and residual saturation of hydrogen in clay-rich sandstone formation: implications for underground hydrogen storage. Int J Hydrogen Energy Feb. 2023;48(13):5175–85. https://doi.org/10.1016/J.IJHYDENE.2022.11.059.
[19] Thaysen EM, et al. Estimating microbial growth and hydrogen consumption in hydrogen storage in porous media. Renew Sustain Energy Rev 2021;151:111481. https://doi.org/10.1016/j.rser.2021.111481.
[20] Pan B, Yin X, Ju Y, Iglauer S. Underground hydrogen storage: influencing parameters and future outlook. Adv Colloid Interface Sci Aug. 2021;294:102473. https://doi.org/10.1016/J.CIS.2021.102473.
[21] Higgs S, et al. In-situ hydrogen wettability characterisation for underground hydrogen storage. Int J Hydrogen Energy 2022;47(26):13062–75. https://doi.org/10.1016/j.ijhydene.2022.02.022.
[22] Jangda Z, et al. Pore-scale visualization of hydrogen storage in a sandstone at subsurface pressure and temperature conditions: trapping, dissolution and wettability. J Colloid Interface Sci Jan. 2023;629:316–25. https://doi.org/10.1016/j.jcis.2022.09.082.
[23] Al-Yaseri A, Abdel-Azeim S, Al-Hamad J. Wettability of water-H_2-quartz and water-H_2-calcite experiment and molecular dynamics simulations: critical assessment. Int J Hydrogen Energy Nov. 2023;48(89):34897–905. https://doi.org/10.1016/J.IJHYDENE.2023.05.294.
[24] Aghaei H, Al-Yaseri A, Toorajipour A, Shahsavani B, Yekeen N, Edlmann K. Host-rock and caprock wettability during hydrogen drainage: implications of hydrogen subsurface storage. Fuel Nov. 2023;351:129048. https://doi.org/10.1016/J.FUEL.2023.129048.
[25] Yekta AE, Manceau JC, Gaboreau S, Pichavant M, Audigane P. Determination of hydrogen–water relative permeability and capillary pressure in sandstone: application to underground hydrogen injection in sedimentary formations. Transport Porous Media Mar. 2018;122(2):333–56. https://doi.org/10.1007/s11242-018-1004-7.
[26] Hashemi L, Glerum W, Farajzadeh R, Hajibeygi H. Contact angle measurement for hydrogen/brine/sandstone system using captive-bubble method relevant for underground hydrogen storage. Adv Water Resour Aug. 2021;154. https://doi.org/10.1016/j.advwatres.2021.103964.
[27] van Rooijen W, Hashemi L, Boon M, Farajzadeh R, Hajibeygi H. Microfluidics-based analysis of dynamic contact angles relevant for underground hydrogen storage. Adv Water Resour Jun. 2022;164:104221. https://doi.org/10.1016/j.advwatres.2022.104221.
[28] Iglauer S, Ali M, Keshavarz A. Hydrogen wettability of sandstone reservoirs: implications for hydrogen geo-storage. Geophys Res Lett Feb. 2021;48(3):e2020GL090814. https://doi.org/10.1029/2020GL090814.
[29] Higgs S, et al. Direct measurement of hydrogen relative permeability hysteresis for underground hydrogen storage. Int J Hydrogen Energy Aug. 2023. https://doi.org/10.1016/J.IJHYDENE.2023.07.270.
[30] Al-Yaseri A, Esteban L, Giwelli A, Abdel-Azeim S, Sarout J, Sarmadivaleh M. Impact of wettability on storage and recovery of hydrogen gas in the lesueur sandstone formation (Southwest hub project, Western Australia). Int J Hydrogen Energy Jul. 2023;48(61):23581–93. https://doi.org/10.1016/J.IJHYDENE.2023.03.131.
[31] Jha NK, Al-Yaseri A, Ghasemi M, Al-Bayati D, Lebedev M, Sarmadivaleh M. Pore scale investigation of hydrogen injection in sandstone via X-ray micro-tomography. Int J Hydrogen Energy Aug. 2021. https://doi.org/10.1016/j.ijhydene.2021.08.042.
[32] Goodarzi S, Zhang Y, Foroughi S, Bijeljic B, Blunt MJ. Trapping, hysteresis and Ostwald ripening in hydrogen storage: a pore-scale imaging study. Int J Hydrogen Energy Feb. 2024;56:1139–51. https://doi.org/10.1016/J.IJHYDENE.2023.12.029.
[33] Nijjer JS, Hewitt DR, Neufeld Ja, Neufeld Ja. Stable and unstable miscible displacements in layered porous media. J Fluid Mech Jan. 2019;869:468–99. https://doi.org/10.1017/jfm.2019.190.
[34] Holtzman R. Effects of pore-scale disorder on fluid displacement in partially-wettable porous media. Sci Rep Oct. 2016;6. https://doi.org/10.1038/srep36221.
[35] Dawe RA, Caruana A, Grattoni CA. Immiscible displacement in cross-bedded heterogeneous porous media. Transport Porous Media Mar. 2011;87(1):335–53. https://doi.org/10.1007/s11242-010-9687-4.
[36] Sajjadi M, Azaiez J. Scaling and unified characterization of flow instabilities in layered heterogeneous porous media. Phys Rev E - Stat Nonlinear Soft Matter Phys Sep. 2013;88(3). https://doi.org/10.1103/PhysRevE.88.033017.
[37] Ringrose P, Bentley M. Reservoir model design. Dordrecht: Springer Netherlands; 2015. https://doi.org/10.1007/978-94-007-5497-3.
[38] Jackson SJ, Agada S, Reynolds CA, Krevor S. Characterizing drainage multiphase flow in heterogeneous sandstones. Water Resour Res 2018;54(4):3139–61. https://doi.org/10.1029/2017WR022282.
[39] Hosseini M, Javaherian A, Movahed B. Determination of permeability index using Stoneley slowness analysis, NMR models, and formation evaluations: a case study from a gas reservoir, south of Iran. J Appl Geophys Oct. 2014;109:80–7. https://doi.org/10.1016/J.JAPPGEO.2014.07.016.
[40] Berg S, Ott H. Stability of CO_2-brine immiscible displacement. Int J Greenh Gas Control 2012;11:188–203. https://doi.org/10.1016/j.ijggc.2012.07.001.
[41] Boon M, Hajibeygi H. Experimental characterization of H_2/water multiphase flow in heterogeneous sandstone rock at the core scale relevant for underground hydrogen storage (UHS). Sci Rep 2022;12. https://doi.org/10.1038/s41598-022-18759-8.
[42] Romano CR, Garing C, Minto JM, Benson SM, Shipton ZK, Lunn RJ. Extreme capillary heterogeneities and in situ fluid compartmentalization due to clusters of deformation bands in sandstones. Int J Greenh Gas Control Mar. 2021;106:103280. https://doi.org/10.1016/J.IJGGC.2021.103280.
[43] Dawe RA, Caruana A, Grattoni CA. Microscale visual study of end effects at permeability discontinuities. Transport Porous Media Jan. 2011;86(2):601–16. https://doi.org/10.1007/s11242-010-9642-4.
[44] Shokri J, et al. Impact of displacement direction relative to heterogeneity on averaged capillary pressure-saturation curves. Water Resour Res Feb. 2022;58(2). https://doi.org/10.1029/2021WR030748.
[45] Jadhawar P, Saeed M. Mechanistic evaluation of the reservoir engineering performance for the underground hydrogen storage in a deep North Sea aquifer. Int J Hydrogen Energy Aug. 2023. https://doi.org/10.1016/j.ijhydene.2023.07.272.

[46] Ngwenya BT, Kwon O, Elphick SC, Main IG. Permeability evolution during progressive development of deformation bands in porous sandstones. J Geophys Res Solid Earth Jul. 2003;108(B7). https://doi.org/10.1029/2002jb001854.
[47] Ngwenya BT, Elphick SC, Main IG, Shimmield GB. Experimental constraints on the diagenetic self-sealing capacity of faults in high porosity rocks. Earth Planet Sci Lett Nov. 2000;183(1–2):187–99. https://doi.org/10.1016/S0012-821X(00)00261-2.
[48] Farrell NJC, Healy D, Taylor CW. Anisotropy of permeability in faulted porous sandstones. J Struct Geol 2014;63:50–67. https://doi.org/10.1016/j.jsg.2014.02.008.
[49] Johnson H, Richards PC, Long D, Graham CC. The geology of the northern North Sea. In: United Kingdom offshore regional report. London, U.K.: HMSO; 1994.
[50] Livera SE. Facies associations and sand-body geometries in the ness formation of the brent group, brent field. Geol Soc, London, Special Publ Jan. 1989;41(1):269–86. https://doi.org/10.1144/GSL.SP.1989.041.01.19.
[51] Singh K, Anabaraonye BU, Blunt MJ, Crawshaw J. Partial dissolution of carbonate rock grains during reactive CO_2-saturated brine injection under reservoir conditions. Adv Water Resour Dec. 2018;122:27–36. https://doi.org/10.1016/J.ADVWATRES.2018.09.005.
[52] Alhosani A, Selem A, Foroughi S, Bijeljic B, Blunt MJ. Steady-state three-phase flow in a mixed-wet porous medium: a pore-scale X-ray microtomography study. Adv Water Resour Feb. 2023;172:104382. https://doi.org/10.1016/J.ADVWATRES.2023.104382.
[53] Hydrogen analysis resource center [Online]. Available: https://h2tools.org/hyarc; 2022.
[54] Chow YTF, Maitland GC, Trusler JPM. Interfacial tensions of ($H_2O + H_2$) and ($H_2O + CO_2 + H_2$) systems at temperatures of (298–448) K and pressures up to 45 MPa. Fluid Phase Equil Nov. 2018;475:37–44. https://doi.org/10.1016/j.fluid.2018.07.022.
[55] Buades A, Coll B, Morel JM. Nonlocal image and movie denoising. Int J Comput Vis Feb. 2008;76(2):123–39. https://doi.org/10.1007/S11263-007-0052-1.
[56] Schluter S, Sheppard A, Brown K, Wildenschild D. Image processing of multiphase images obtained via X-ray microtomography: a review. Water Resour Res 2014. https://doi.org/10.1002/2014WR015256.
[57] Raeini AQ, Bijeljic B, Blunt MJ. Generalized network modeling: network extraction as a coarse-scale discretization of the void space of porous media. Phys Rev E Jul. 2017;96(1). https://doi.org/10.1103/PhysRevE.96.013312.
[58] Dong H, Blunt MJ. Pore-network extraction from micro-computerized-tomography images. Phys Rev E - Stat Nonlinear Soft Matter Phys Sep. 2009;80(3). https://doi.org/10.1103/PhysRevE.80.036307.
[59] Bultreys T, et al. Validation of model predictions of pore-scale fluid distributions during two-phase flow. Phys Rev E 2018;97:53104. https://doi.org/10.1103/PhysRevE.97.053104.
[60] Patsoukis Dimou A, Menke HP, Maes J. Benchmarking the viability of 3D printed micromodels for single phase flow using particle image velocimetry and direct numerical simulations. Transport Porous Media Jan. 2022;141(2):279–94. https://doi.org/10.1007/s11242-021-01718-8.
[61] Menke HP, Maes J, Geiger S. Upscaling the porosity–permeability relationship of a microporous carbonate for Darcy-scale flow with machine learning. Sci Rep Dec. 2021;11(1). https://doi.org/10.1038/s41598-021-82029-2.
[62] Maes J., Menke H.P. A bespoke OpenFOAM toolbox for multiphysics flow simulations in pore structures ICFD2020.
[63] Soulaine C, et al. The impact of sub-resolution porosity of X-ray microtomography images on the permeability. Transport Porous Media 2016;113(1):227–43. https://doi.org/10.1007/s11242-016-0690-2.